aerospace

MDPI

Article

Thermal Radiation Analysis Method and Thermal Control System Design for Spaceborne Micro-Hyperspectral Imager Operating on Inclined-LEO

Xinwei Zhou [1], Yutong Xu [2], Yongnan Lu [3], Yangyang Zou [4], Hanyu Ye [1] and Tailei Wang [1,*]

[1] School of Optoelectronic Engineering and Instrumentation Science, Dalian University of Technology, Dalian 116024, China; zhouxinwei@dlut.edu.cn (X.Z.)
[2] School of Instrumentation & Electrical Engineering, Jilin University, Changchun 130061, China
[3] School of Optoelectronic Engineering, Changchun University of Science and Technology, Changchun 130022, China
[4] School of Artificial Intelligence, Changchun University of Science and Technology, Changchun 130022, China
* Correspondence: tlwang@dlut.edu.cn

Abstract

Thermal control of spaceborne micro-hyperspectral imagers (MHIs) operating in inclined low-Earth orbits (LEOs) presents significant challenges due to the complex and dynamically varying external heat flux, which lacks a stable heat dissipation surface. This study proposes a thermal radiation analysis method capable of rapidly deriving accurate numerical solutions for the thermal radiation characteristics of spacecraft in such orbits. A dedicated thermal control system (TCS) was designed, featuring a radiator oriented towards the $+z_s$ plane, which was identified as having stable and low incident heat flux across extreme solar–orbit angle conditions. The system employs efficient thermal pathways, including thermal pads and a flexible graphite thermal ribbon, to transfer heat waste from the imaging module to the radiator, supplemented by electric heaters and multilayer insulation for temperature stability. Steady-state thermal analysis demonstrated excellent temperature uniformity, with gradients below 0.017 °C on critical optics. Subsequent thermo-optical performance analysis revealed that the modulation transfer function (MTF) degradation was maintained below 2% compared to the ideal system. The results confirm the feasibility and effectiveness of the proposed thermal design and analysis methodology in maintaining the stringent thermo-optical performance required for MHIs on inclined-LEO platforms.

Keywords: remote sensing satellite; spaceborne hyperspectral imager; thermal radiation; thermal control system; thermo-optical performance analysis

Check for updates

Academic Editor: Hyun-Ung Oh

Received: 4 November 2025
Revised: 6 December 2025
Accepted: 10 December 2025
Published: 27 December 2025

Copyright: © 2025 by the authors. Licensee MDPI, Basel, Switzerland. This article is an open access article distributed under the terms and conditions of the Creative Commons Attribution (CC BY) license.

1. Introduction

With the development of modern space optical remote sensing technology, the requirements for the functions and performance of space optical payloads are increasing [1]. In recent years, the development of satellite-based spectral imagers has received widespread attention, which can integrate spatial, radiometric, and spectral information on geographical targets, greatly enhancing the information dimension of Earth observation [2]. For providing in-depth observation, resource data, and emergency reference for national citizenry and national defense areas, on the one hand, a spectral imager should be responsive, lightweight, and low-cost [3]; on the other hand, it must also be able to provide hyperspectral image information of ground targets for more accurate feature identification. However,

conventional spectral imagers [4] are unable to satisfy the above missions synchronously; hence, there is an urgent need for a novel micro-hyperspectral imager on-board a small satellite and operating in an untypically inclined near-Earth orbit to break through the above technical barriers, which has the coverage characteristics for rapid revisit observations at low latitudes.

A novel space micro-hyperspectral imager (MHI) based on computational hyperspectral theory attempts to achieve simultaneous improvements in spatial, spectral, and temporal resolution with optical payload as well as spectral inversion techniques [5,6]. Unlike multispectral imagers [7], hyperspectral imagers can acquire target spectral information in dozens or even hundreds of spectral bands simultaneously [8,9]. This requires additional processors and electronics to handle the massive grayscale data. For micro Earth observation satellites (MEOSs)—where energy and mass are strictly limited [10]—the waste heat generated by these components imposes significant challenges on thermal design, making it one of the most critical drivers for MHI development. The cosmic cold background, celestial radiation heat flux, and internal equipment heat generation are the main sources of temperature disturbance for space optical instruments. The purpose of thermal design is to manage the internal and external thermal equilibrium of a spacecraft; hence, the thermal control system (TCS) is used to ensure that critical optical components achieve the suitable temperature metrics [11,12].

In the past, many thermal control system designs have been proposed and studied for different space optical instruments. The total thermal control power of the high-resolution imaging camera on China's first Mars exploration Tianwen-1 mission [13] and a light off-axis space optical remote sensor [14] reach 87 W and 47 W, respectively. Radiators with large areas are utilized for heat dissipation of electronic components on eROSITA [15] and GF-4 [16,17]. It follows that one of the distinguishing features of space optical instruments carried on large satellites is that they have an adequate mass budget, surface area, and energy source, and therefore provide sufficient margin to the TCS. However, a thermal design approach applicable to small space optics instruments, which uses rationally designed radiators and is complemented by efficient active and passive thermal control systems, is necessary for small satellites. Yang et al. proposed a quasi-all-passive TCS for the Luojia 1-01 satellite, which stabilized the temperature of the two small cameras at 12 °C [18]. Jiang et al. designed a radiator to optimize the heat diffusion for CCD and PTC; the structural configuration of star sensors and the geometrical parameters and coating material characteristics of radiators on heat diffusion were investigated by heat flux analysis. This design is validated by simulation analysis and experiments on orbit, and the temperatures of three star sensors are from 17.8 °C to 19.6 °C [19].

Most existing studies focus on space optical instruments in sun-synchronous orbits, geostationary orbits, or for deep space exploration [20,21]. Their thermal design and analysis methods are not applicable to spacecraft in non-typical inclined orbits. The illumination environment of non-typical inclined-LEO is extremely complex, mainly due to the ascending node equinox drift and Earth's rotation. These factors cause periodic variations in the angle between the orbital plane and the solar vector, leading to the lack of a stable heat dissipation surface. Additionally, the magnitude of incident heat flux is directly related to the spacecraft's attitude and orbital parameters. At present, there are few existing reports on studies related to the TCS of space optical instruments operating in inclined-LEO; to date, only Bai et al. [22] conducted thermal design studies, but they did not study in-depth the external heat flux calculation method and did not consider the special working conditions caused by the sun–orbit angle.

To address this research gap, we propose a method for rapidly deriving accurate numerical solutions for the thermal radiation characteristics of inclined-LEO spacecraft.

This approach can serve as a design basis for the thermal control systems (TCSs) of satellites and their payloads. Concurrently, we verify the methodology's validity through thermo-optical performance analysis. The manuscript is structured as follows: Section 2 details the study methodology; Section 3 presents the developed TCS for the spaceborne MHI and the thermo-optical performance analysis framework; Section 4 discusses the results; and Section 5 summarizes the conclusions, findings, future research directions, and limitations.

2. Methodology

2.1. Satellite Attitude and Orbit

To identify the incident heat flux of the satellite, the definition of the orbit and attitude based on the coordinate system is given in Figure 1. In describing the parameters of inclined-LEO, the equatorial coordinate system $O - XYZ$ and the orbital coordinate system $O - x_o y_o z_o$, which are Cartesian coordinate systems that follow the right-hand law, are chosen with the center at the geocentric. Moreover, the payload coordinate system is extremely close in position and in the same direction as the satellite coordinate system; hence, the two coordinate systems are considered to overlap as $o - x_s y_s z_s$ when neglecting the installation error matrix.

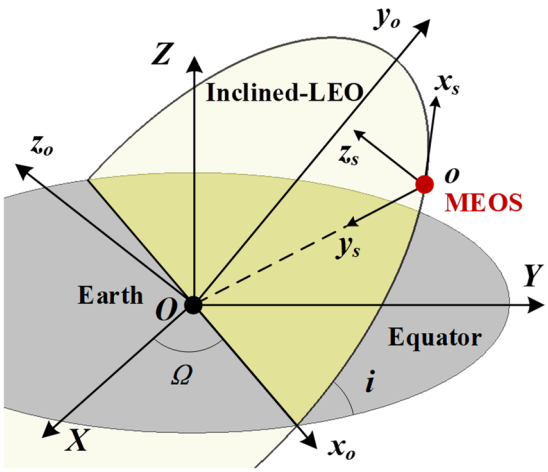


Figure 1. Definition of attitude, orbit, and coordinate system. Ω and i represent the ascending node equinox and orbital inclination, respectively. The equatorial coordinate system $O - XYZ$ is an inertial coordinate system, the $X - Y$ plane is in the equatorial plane of the Earth, the X-axis points to the equinox, the Z-axis points to the north celestial pole, and the Y-axis conforms to the right-hand rule. The center of the orbital coordinate system $O - x_o y_o z_o$ coincides with the equatorial coordinate system, the $x_o - y_o$ plane is in the orbital plane, the x_o-axis points to the ascending node, the z_o-axis points to the orbital plane normal, and the y_o-axis conforms to the right-hand rule. The satellite coordinate system $o - x_s y_s z_s$ is solidly connected to the satellite, the $x_s - y_s$ plane is in the orbital plane, the x_s-axis points to the direction of flight, the y_s-axis points to the center of the earth, and the z_s-axis points to the normal direction of the orbital plane.

According to the coordinate transformation theory, set the Euler angles of the three axes be θ, φ, and ψ, respectively. The coordinate transformation matrices around the three axes from the orbital coordinate system $O - x_o y_o z_o$ to the satellite coordinate system $o - x_s y_s z_s$ are expressed as R_{os}^{x}, R_{os}^{y}, and R_{os}^{z}, respectively. The on-orbit attitude of the MHI is Earth-directed and three-axis stable, i.e., the optical axis points to the geocentric regardless of the imaging mission or regular flight. Therefore, the satellite coordinate system can be considered to rotate around the Z-axis of the orbital coordinate system during

one orbital period. Then, the transformation matrix from the orbital coordinate system to the satellite coordinate system at any moment τ is as follows

$$R_{os} = R_{os}^{x} \cdot R_{os}^{y} \cdot R_{os}^{z} = \begin{bmatrix} \cos(-2\pi \cdot \tau/T) & \sin(-2\pi \cdot \tau/T) & 0 \\ -\sin(-2\pi \cdot \tau/T) & \cos(-2\pi \cdot \tau/T) & 0 \\ 0 & 0 & 1 \end{bmatrix} \quad (1)$$

where T represents the orbital period.

2.2. Modeling of the Solar Vector

The solar vector can be characterized by the solar-orbit angle β, the junction angle γ_Ω, and the phase angle Φ, which are continuously changing with the satellite flight and the Earth-sun geometry relationship. As shown in Figure 2, in the orbiting sphere coordinate system, the coordinates of the sun vector are $(\Theta, \Gamma, r)^T$. Further, in this coordinate system, there is the following

$$\begin{cases} \sin\beta = \cos i \sin\delta_\theta + \sin i \cos\delta_\theta \sin(\Omega - \alpha_\theta) \\ \gamma = 2\pi(\tau - \tau_\Omega - (\gamma_\Omega/2\pi)\tau_o)/\tau_o \\ \cos\Phi = \cos\beta\cos\gamma \end{cases} \quad (2)$$

where γ_Ω represents the ascending-junction angle. α_θ and δ_θ represent the solar right ascension and declination, respectively. Then, based on the transformation theory between spherical and right-angle coordinate systems, the coordinates of the solar vector in the orbital coordinate system are as follows

$$\mathbf{S} = (\cos\beta\sin(\gamma - \gamma_\Omega), \cos\beta\cos(\gamma - \gamma_\Omega), \sin\beta)^T \quad (3)$$

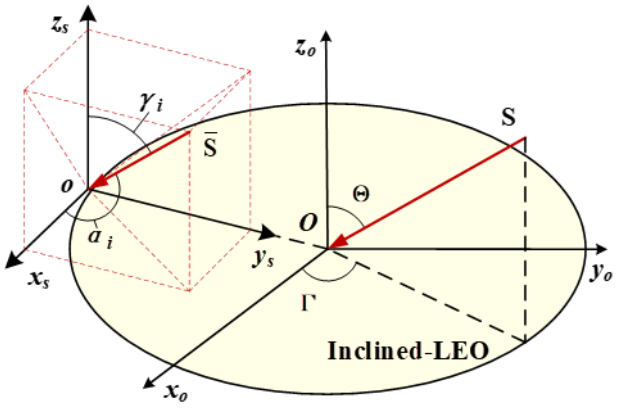


Figure 2. Description of the solar vector. α_i, β_i and γ_i represent the angles of the solar vector $\bar{\mathbf{S}}$ in the satellite coordinate system with respect to each coordinate axis, respectively.

According to Equations (1)–(3), at any moment τ, the solar vector $\bar{\mathbf{S}}$ in the satellite coordinate system can be expressed as follows

$$\bar{\mathbf{S}} = R_{ob}^{c} \cdot R_{ob} \cdot \mathbf{S}_o = \begin{bmatrix} -\cos\beta\sin\theta\sin(2\pi \cdot \tau/T) - \cos\beta\sin\theta\cos(2\pi \cdot \tau/T) \\ \cos\beta\sin\theta\cos(2\pi \cdot \tau/T) - \cos\beta\cos\theta\sin(2\pi \cdot \tau/T) \\ \sin\beta \end{bmatrix} \quad (4)$$

where R_{os}^{c} represents the coordinate transformation matrix for the initial moment (MEOS through the ascending intersection). In the satellite coordinate system, the directional cosine expressions of the angle between the sun vector and each coordinate axis are as follows

$$\begin{cases} \cos\alpha_i = \cos\left\langle r_{xo} \cdot \bar{\mathbf{S}} \right\rangle = \frac{r_{xo}\bar{\mathbf{S}}}{|r_{xo}||\mathbf{S}|} \\ \cos\gamma_i = \cos\left\langle r_{zo} \cdot \bar{\mathbf{S}} \right\rangle = \frac{r_{zo}\bar{\mathbf{S}}}{|r_{zo}||\mathbf{S}|} \end{cases} \tag{5}$$

where r_{xo}, r_{yo}, and r_{zo} represent the unit direction vector of each coordinate axis, respectively; α_i and γ_i represent the azimuth angle and zenith angle, respectively. Equation (5) presents the relative position of the satellite to the Sun.

2.3. Analysis of Space Thermal Radiation

2.3.1. Direct Solar Radiation

Direct solar radiation is the most dominant space thermal radiation received by spacecraft operating in LEO, and solar rays are considered as uniform and parallel beams in orbital thermal analysis. As shown in Figure 3, the direct solar radiation flux dq_1 on the surface dA of any MEOS micro-element in the satellite coordinate system is as follows:

$$dq_1 = |S| \cos\beta_s dA \tag{6}$$

where β_s represents the angle between the solar vector and the dA normal vector $\vec{n}$, and $|S|$ represents the solar constant. Set ϕ_1 be the direct solar radiation coefficient, and $\phi_1 = \cos\beta_s$.

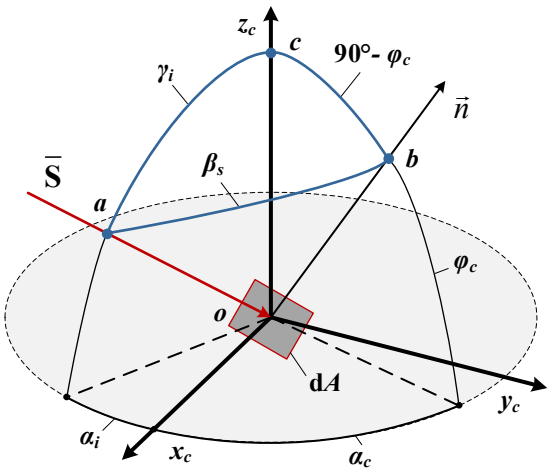


Figure 3. Direct solar radiation coefficient analysis. The points a, b, and c form a spherical triangle Δabc, so $\angle aob$, i.e. β_s, can be expressed by the cosine formula of spherical triangle sides.

Direct solar radiation is not only related to the coordinates of the solar vector in the satellite coordinate system but also to the satellite flight attitude. Therefore, the satellite coordinate system is converted into a spherical coordinate system, and based on the spherical trigonometric cosine equation, it can be derived as follows

$$\phi_1 = \sin\alpha_c \cos\gamma_i + \cos\alpha_c \sin\gamma_i \cos(\varphi_c - \alpha_i) \tag{7}$$

where $(\varphi_c, \alpha_c)^T$ represents the coordinate of the micro-element normal vector in the satellite spherical coordinate system.

2.3.2. Earth IR and Albedo

The radiant energy projected onto the Earth by the Sun is partially absorbed by the Earth, and the absorbed energy is dissipated into space in the form of infrared radiant energy. In general, the Earth is considered to be a uniformly radiating thermal equilibrium, i.e., the intensity of infrared radiation (IR) is the same at any point on Earth. The heat flux of the Earth IR received on any micro-element of the satellite is as follows

$$dq_2 = \frac{1-\rho}{4}|S|\phi_2 \tag{8}$$

where ρ represents the average albedo ($\rho = 0.3$), and ϕ_2 represents the Earth IR coefficient. Even with a reasonable fluctuation in albedo, the power redundancy and integrated active–passive temperature regulation strategy of the thermal control system used in this study can effectively adapt, ensuring temperature stability of critical optical components and opto-mechanical structures.

In addition, Earth albedo heat flux is a small proportion of total space thermal radiation absorbed by the satellite; hence, the Earth albedo radiation coefficient ϕ_3 can be approximated as follows

$$\phi_3 = \phi_2 \cos\Phi \tag{9}$$

Therefore, the Earth albedo heat flux on any micro-element of the satellite in the non-shaded region is as follows

$$dq_3 = \rho|S|\phi_3 \tag{10}$$

2.4. Calculation of Incident Heat Flux

MEOS operates at an orbital altitude of 520 km and an orbital inclination of 45°. Assuming a service period from 1 June 2022 to 1 June 2025, the solar–orbit angles for this period are presented in Figure 4, where the maximum solar–orbit angle is $\beta = 68.402°$ and the minimum solar–orbit angle is $\beta = -67.984°$. These two typical extreme cases, presented in Table 1, correspond to the two possible extreme solar–orbit angles. The assumption of uniform Earth IR and albedo is fundamental in spacecraft thermal analysis and widely adopted in aerospace engineering, whose introduced errors are negligible for the thermal control system design of conventional spacecraft like satellites.

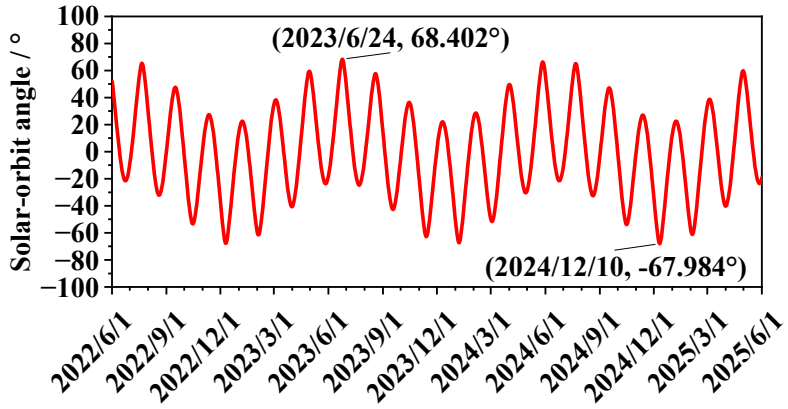
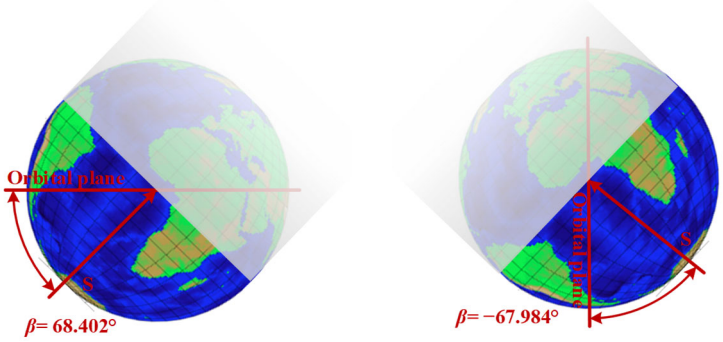


Figure 4. Solar–orbit angle.

Table 1. Typical extreme cases.

	Case-I	Case-II
Data	24 June 2023	10 December 2024
β	68.402°	−67.984°
Solar constant	1323.3 W/m^2	1408.9 W/m^2
Solar vector		

It can be seen from Table 1 that in two typical extreme cases (Case-I and Case-II), the solar–orbit angle in the orbital coordinate system exhibits two completely opposite characteristics, which are approximately symmetric along the orbital plane. Therefore, it is necessary to analyze the two cases separately. The variations in the azimuth and zenith angles of the solar vector in the satellite spherical coordinate system during an orbital period is calculated based on Equation (7) and presented in Figure 5. It can be seen that the azimuthal angle of the solar vector remains constant, on the contrary, the zenith angle of the solar vector continuously changes due to MEOS's Earth-oriented attitude. In addition, the coordinate variations in the two cases are considerably different due to the difference in solar–orbit angle.

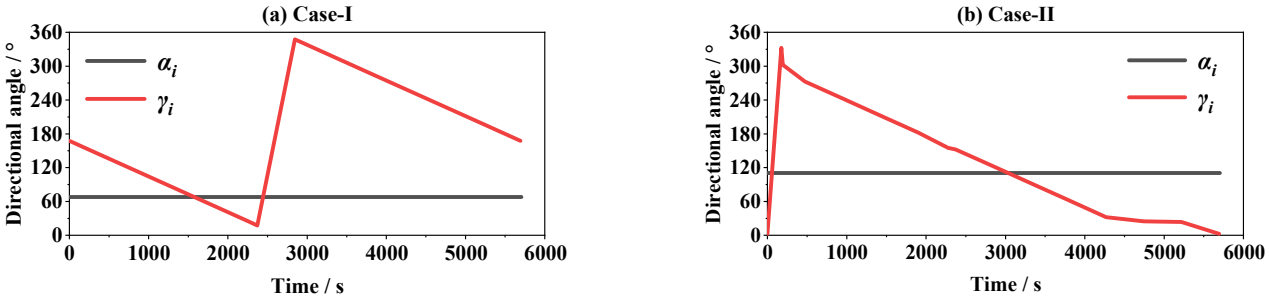


Figure 5. The spherical coordinates of the solar vector: (**a**) Case-I and (**b**) Case-II.

However, the solar vector alone still does not visualize the space thermal radiation on the individual envelopes of MEOS. Therefore, for both cases, according to Equations (6) and (7) and Table 1, the direct solar radiation heat fluxes within one orbital period (taking the ascending intersection point as the starting point of the MEOS flight) are calculated and presented in Figure 6a,b. The Earth IR heat fluxes and Earth albedo heat fluxes are also calculated according to Equations (8)–(10) and presented in Figure 6c–f. After comparing the two cases, the results indicate that both direct solar and Earth albedo heat fluxes appear to be deflected in the time domain owing to the fact that the directional flip of the Sun–orbit angle of the inclined orbit; on the contrary, Earth IR remains consistent in both cases due to its independence from solar vector coordinates.

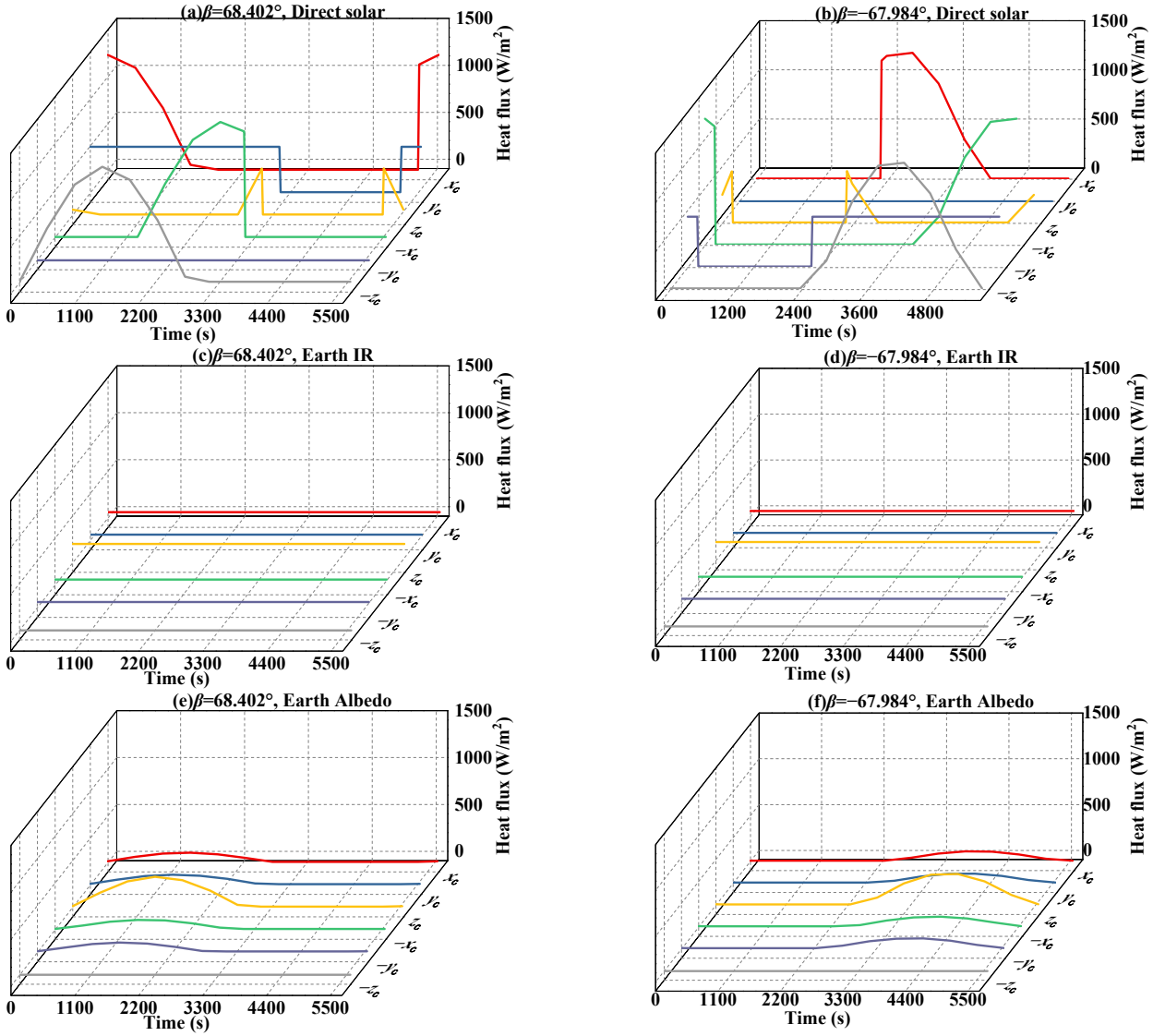


Figure 6. Incident heat flux of the MEOS envelope. (**a**) Direct solar radiation of Case-I. (**b**) Direct solar radiation of Case-II. (**c**) Earth IR of Case-I. (**d**) Earth IR of Case-II. (**e**) Earth albedo of Case-I. (**f**) Earth albedo of Case-II.

In the insolation zone, in the $+x_s$ and $-x_s$ planes of MEOS, a drastic change in direct solar radiation occurs, with a peak heat flux of 1283.7 W/m^2; similarly, the $-z_s$ plane peaks at 1283.7 W/m^2. Moreover, when $\beta = 68.402^\circ$, the heat flux of direct solar radiation in the -y plane is 0, while more than half of the orbital period in the $+y_s$ plane remains at 486 W/m^2. Conversely, when $\beta = -67.984^\circ$, the heat flux of direct solar radiation in the $-y_s$ plane is 0, while more than half of the orbital period in the $-y$ plane remains at 507.2 W/m^2. As a result, only the direct solar heat flux in the $+z_s$ plane is small and has only two brief and low amplitude peaks. On the other hand, the Earth IR heat flux is low and constant for each envelope surface; the variation of Earth Albedo is flat and small in magnitude. In summary, for the most extreme cases of fluctuating sun-orbit angles throughout the year, the $+z_s$ plane has a small amplitude and smooth incident heat flux all year round, which is suitable to be utilized as a radiator for the MHI waste heat, with the advantage of not having to equip a complex radiator with variable orientation and without frequent satellite maneuvers.

3. Application

3.1. The Space Micro-Hyperspectral Imager and Thermo-Optical Performance Analysis

To achieve both high-resolution and hyperspectral imaging, we developed a new micro-hyperspectral imager (MHI) with meter-level spatial resolution and nanometer-level spectral resolution (Figure 7a). Carried on a micro Earth observation satellite (MEOS), the MHI mainly comprises two components: a telescope system and an imaging module. The telescope system is a typical Ritchey–Chrétien design with an optical aperture exceeding 120 mm, including the primary mirror (PM), secondary mirror (SM), and focal plane corrector (FPC). Its performance directly determines MHI imaging quality; thus, these optical components have stringent tolerances. The imaging module—equipped with a driver circuit, image processing circuit, and filtered CMOS sensor—receives the converged and corrected optical signals from the telescope. During operation, the module's processors (FPGA-I, FPGA-II) and CMOS sensor generate considerable waste heat while performing high-resolution and hyperspectral imaging tasks.

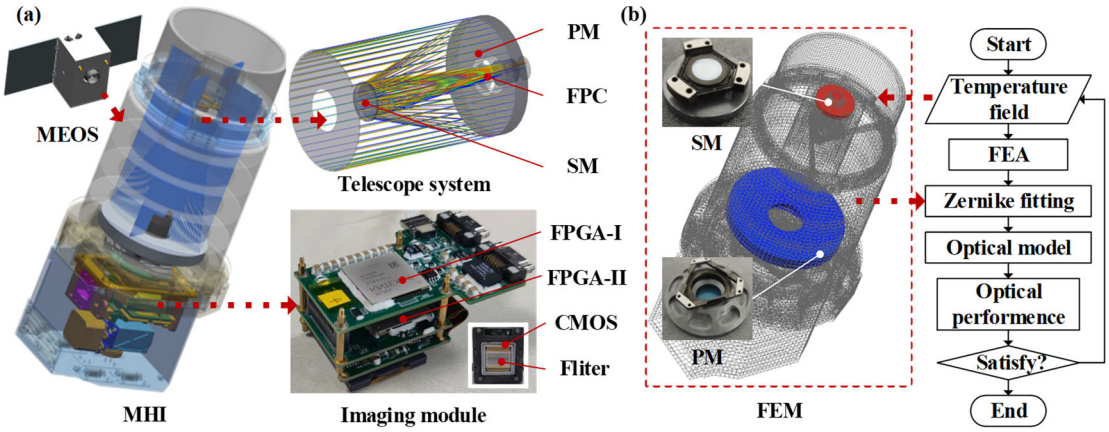


Figure 7. Background of MHI. (**a**) Components of the MHI. (**b**) Thermo-optical performance analysis: The finite element model for STOP analysis adopts 2D shell elements (thin-walled structures) and 3D tetrahedral elements (optics/key opto-mechanics), with 177,958 total elements and 311,746 nodes. Thermal boundary conditions use steady-state temperature loads, and structural constraints apply 6-DOF fixed constraints at the base mounting points. Mechanical contacts are modeled as bonded contacts, while bonding interfaces use shared nodes to ensure thermal–mechanical continuity.

The causes of optical aberrations are mainly degradation of optics and deformation of the metering structure. Although the opto-mechanisms are designed to be athermalization [23,24], the continuous accumulation of waste heat generated by the imaging module can exceed the thermal adaptation of the opto-mechanisms and lead to degradation in MHI imaging quality. As shown in Figure 7b, the structure–thermal–optical performance (STOP) analysis is used to predict the on-orbit thermo-optical performance of the MHI. First, the temperature field is applied to the finite element model (FEM) of the MHI, and finite element analysis (FEA) is performed; then, the optical surface data results are substituted into the optical model based on Zernike-fitting technique; finally, the characterized optical properties of the MHI are evaluated.

3.2. Design of Thermal Control System

On orbit, when the MHI performs imaging missions, the imaging module CMOS converts the optical signal, and the imaging module circuitry processes a massive amount of image data, which generates waste heat that is transferred to the telescope system in the form of both conduction and radiation. In this case, the suddenly applied thermal

loads cause temperature fluctuations in optics. This temperature fluctuation will be more dramatic when the optical instrument is micro due to its small thermal inertia (the total heat capacity of the MHI is only 4500 J/K). Therefore, in the development of thermal control systems for space optical instruments, the primary concern is to design reasonable radiators to discharge waste heat.

Based on the calculated results of the space heat radiation in Figure 6, it can be concluded that the incident heat flux is relatively low in the +Y plane, -Y plane and +Z plane of MEOS; however, the direct solar heat flux characteristics in the +Y and -Y planes are switched due to the change in the β angle of the inclined orbit. Therefore, the +Z-oriented plane with stable incident heat flux is chosen as the radiator orientation considering the robustness and reliability of the thermal design. Further, the window area of the radiator is determined by the following heat balance equation

$$Q_{out} + Q_{in}\alpha_s A = \varepsilon_h \sigma_p T^4 AF \tag{11}$$

where Q_{in} is the average power consumption of the imaging module over an orbital period; Q_{out} is the average incident heat flux of the radiator over an orbital period (the values are derived from Figure 6); A is the window area of the radiator; α_s is the Stefan–Boltzman constant, which is $\alpha_s = 5.67 \times 10^{-8} \mathrm{W}/\left(\mathrm{m}^2 \cdot \mathrm{K}^4\right)$; T is the temperature of the heat sink surface; and F s the viewing angle factor (GVBF), where $F \approx 1$.

To improve heat accumulation within the imaging module, as shown in Figure 8, all heat-generating components first transfer heat efficiently to the nearest aluminum alloy electrical enclosure via thermal pads. These pads achieve a heat transfer coefficient of 3000 $\mathrm{W/m^2}$ between the two interfaces. After assembly, the combined housing surfaces form a flat plane that serves as a heat collection surface. Heat is then transferred via another thermal pad to a flexible thermal ribbon, which is constructed by stacked graphite films. This ribbon not only directs heat from the source to a designated location but also possesses sufficient flexibility to avoid interfering with the operation of the focusing mechanism. On the one hand, the imaging module's heat is conducted to the heat sink via the aforementioned heat transfer paths. On the other hand, the structural thermal mass of the back-hood and optical bench increases the module's thermal inertia, effectively suppressing temperature fluctuations.

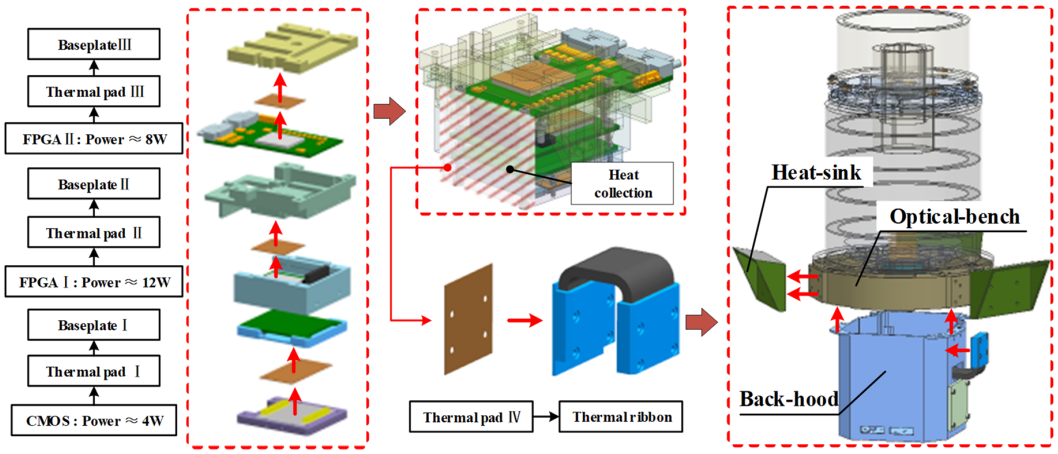


Figure 8. Heat transfer pathways. Each imaging module operates for 300 s per track, during which the CMOS operates at 4 W power and 2506 $\mathrm{W/m^2}$ heat flux density for hyperspectral data acquisition; FPGA-I operates at 12 W with a heat flux density of 21,390 $\mathrm{W/m^2}$ to drive the CMOS; FPGA-II operates at 8 W with a heat flux density of 14,260 $\mathrm{W/m^2}$ to process hyperspectral data. The total heat dissipation on the heat collection surface is 24 W, with a heat flux density of 114,832 $\mathrm{W/m^2}$.

From Equation (11), it is evident that the heat dissipation surface area depends on the load's heat generation power, the performance of the thermal control coating, and the external heat flux received. Therefore, based on the temperature control specifications and thermal control parameters, calculations indicate that the total surface area of the F46 secondary surface mirror (emissivity/absorptivity = 0.9/0.1) heat sinks for the three heat sinks is 0.9 m^2. For Earth-oriented spacecraft with three-axis stable attitude, minor attitude deviations have minimal impact on the incident heat flux characteristics of the selected $+z_s$-plane radiator, and the thermal control system is designed with power redundancy that, combined with its temperature regulation strategy, can fully cope with disturbances such as errors in thermal radiation calculation and small attitude deviations.

3.3. Thermal Compensation Method

While the thermal equilibrium temperature can be controlled by adjusting the radiator's heat dissipation area, the instrument's temperature tends to drop during orbital periods without imaging tasks. Therefore, it is necessary to compensate for the instrument's heat loss to ensure compliance with temperature specifications during both active and inactive phases of a single in-orbit mission. The following active and passive thermal control methods are applied to the instrument:

(1) Considering constraints on the size of the microsatellite control system circuit board, the imager employs an integrated thermal control configuration rather than a modular one. Consequently, electric heaters and multilayer components are deployed only on the exterior of the primary optical-mechanical structure to achieve internal thermal homogenization. The primary and secondary covers do not participate in imaging and thus maintain lower temperature levels than the imaging unit. They are thermally isolated from the imaging unit body via thermal pads made of polyimide with a thermal conductivity of only 0.32 W/(m·K).

(2) Based on the optical-mechanical structure characteristics of the imager, a total of six polyimide film-type electric heaters are bonded to the outer surfaces of the primary cover, support wings, secondary mirror, metrology structure, platform, and rear cover. According to mission requirements, the total peak power and long-term power of all heaters are limited to 8 W and 5 W, respectively.

(3) Each heater group is paired with a negative temperature coefficient thermistor for real-time temperature monitoring of controlled components. The control strategy employs proportional controllers for PWM temperature regulation across all heaters. However, when the imaging module is active, heaters on the platform and rear cover are powered down to limit overall peak power consumption and reduce satellite power demands. The thermal control system reserves sufficient design margin through radiator area margin, power redundancy, and PWM dynamic temperature regulation strategy, which can fully cope with theoretical modeling errors and reasonable uncertainties of environmental parameters, in line with industry practice for spacecraft thermal control design.

(4) To mitigate radiation heat exchange with space and the satellite, the imaging instrument's entire outer surface is encapsulated with a multilayer thermal insulation assembly. This consists of 20 layers of double-sided aluminum-coated polyurethane film, achieving an equivalent thermal conductivity on the order of 10^{-4} W/(m·K). The F46 secondary surface mirror is employed as the multilayer surface layer, while nylon mesh is used as the spacer layer.

4. Results and Discussion

As shown in Figure 9, based on the thermal control system design, the on-orbit steady-state temperature fields of the MHI under two typical operating conditions were analyzed

by NX TMG. Steady-state thermal analysis indicates that the imaging system's temperature levels converge. In Case-I, the primary mirror's temperature range is 18.758–18.76 °C, with a temperature gradient of 0.002 °C; the secondary mirror's temperature range is 18.6208–18.6377 °C, with a temperature gradient of 0.0169 °C. In Case-II, the primary mirror's temperature range is 18.7584–18.7604 °C, with a temperature gradient of 0.002 °C; the secondary mirror's temperature range is 18.6220–18.6388 °C, with a temperature gradient of 0.0119 °C. Additionally, other opto-mechanisms satisfy temperature tolerance requirements, providing stable support for optical elements. Both optical components and other opto-mechanical structures satisfy the MHI's temperature tolerance specifications, with extremely minimal temperature gradients across individual components. The maximum temperature deviation for any optical element is only 1.379 °C, occurring on the secondary mirror. The favorable temperature conditions maintain the surface profile and curvature of optical surfaces, while the minimal temperature gradients prevent the optical system from generating unpredictable higher-order aberrations. The temperature distributions of the imager under two typical operating conditions are remarkably similar, with temperature levels and gradients being extremely close—temperature differences across all dimensions remain within 0.1 °C. This demonstrates that the radiator effectively assists the imager in coping with the extreme thermal environment of an inclined low-Earth orbit while maintaining a consistent thermal environment.

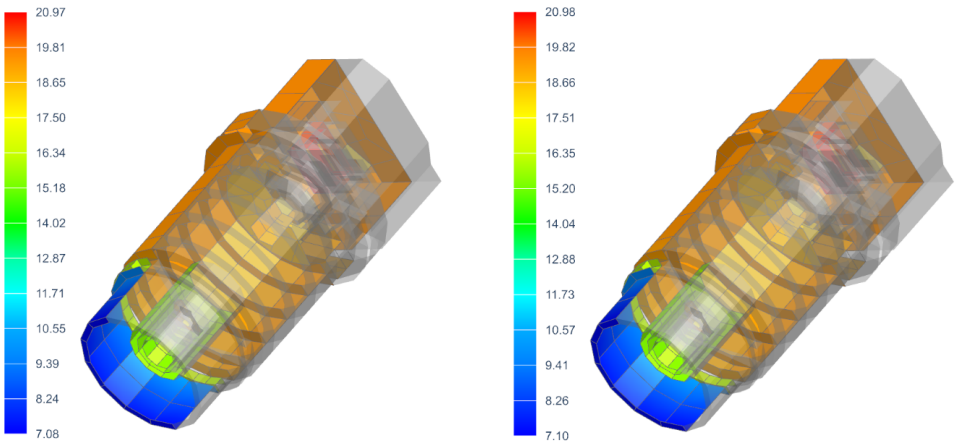
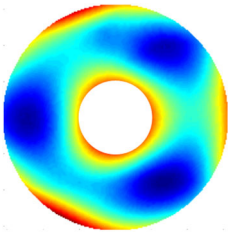
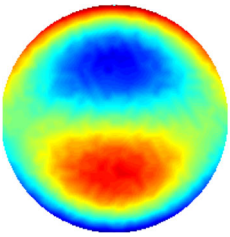
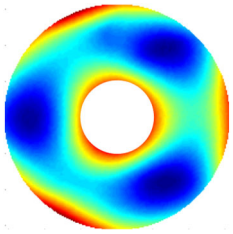
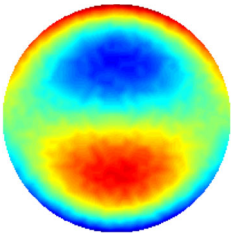


Figure 9. Steady-state thermal analysis (unit: °C): (**a**) Case-I and (**b**) Case-II.

In Figure 7b, the thermo-optical analysis method is established, and by means of the temperature mapping interface technology, the on-orbit temperature field can be mapped to the finite element model, which is then subjected to the thermo-solid-coupled finite element analysis by NX Nastran. The results of misalignment, radius of curvature (ROC), and surface shape are shown in Table 2. It can be seen that the performance of the opto-mechanism is well maintained and that the two typical conditions are extremely close to each other, indicating that the thermal radiation method can guarantee the normal operation of the MHI optical elements. Further, we characterized the MHI's optical performance using Zemax OpticStudio, considering the effects of the on-orbit temperature field: optical element misalignment, surface shape degradation, and lens refractive index changes. As shown in Figure 10, relative to the ideal optical system modulation transfer function (MTF), which is 0.33 at a spatial frequency of 118 lp/mm for the central field of view (FOV = 0°), the degradation caused by the thermal control system in both cases is less than 2% (Case-I is 0.324, while Case-II is 0.326). Such a level of optical performance degradation is considered negligible in the field of remote sensing satellites. Therefore, the thermal radiation analysis

method and thermal control system design proposed in this paper for the MHI operating in inclined-LEO are feasible.

Table 2. Optical performance results.

Performance	Case-I		Case-II	
	PM	**SM**	**PM**	**SM**
Misalignment (μm)	Datum	0.1	Datum	0.104
ROC (μm)	3.05	0.407	3.1	0.409
Surface shape (RMS, nm)				
	0.155	0.003	0.15	0.003

The design tolerances for misalignment, ROC, and surface shape are 5 μm, 1 mm, and 12.6 nm, respectively.

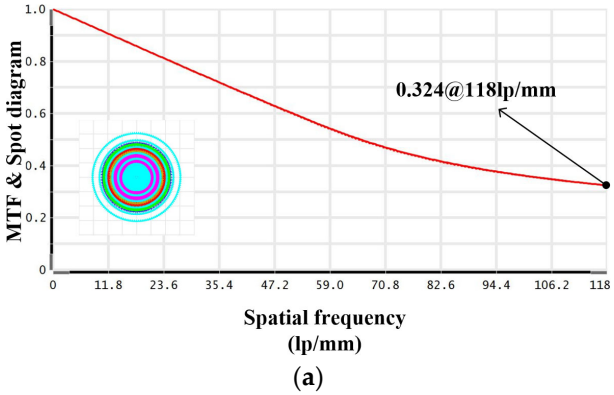


Figure 10. Results of MTF (FOV = 0°): (**a**) Case-I and (**b**) Case-II.

5. Conclusions

This study has comprehensively addressed the thermal control challenges associated with a micro-hyperspectral imager operating in a dynamically complex inclined low-Earth orbit. The work establishes a systematic framework, encompassing a rapid thermal radiation analysis method and a validated thermal control system design, which collectively ensure the instrument's stringent thermo-optical performance. The specific conclusions are delineated as follows:

First and foremost, by rigorously modeling orbital mechanics, satellite attitude, and the celestial geometry of the Sun and Earth, this method provides an approach for calculating the time-varying external heat fluxes—direct solar, Earth IR, and albedo—for spacecraft in arbitrary near-Earth orbits. The methodology presented in this paper is inherently universal and can serve as fundamental research to guide the thermal radiation analysis and thermal design work for the vast majority of low-Earth orbit spacecraft, irrespective of their specific orbital inclination or altitude. The successful application to a challenging 45° inclined orbit underscores its broad applicability.

Second, guided by this analytical method, an efficient thermal control system was designed, centering on the strategic selection of the $+z_s$-oriented plane as a stable radiator. This decision, derived directly from the generic heat flux calculations, proved robust against the extreme seasonal variations in the solar–orbit angle. The design incorporates optimized

heat transfer pathways using thermal pads and flexible graphite ribbons to manage high heat flux densities from internal electronics, effectively mitigating the risks posed by the payload's low thermal inertia.

Finally, steady-state thermal analysis under two extreme orbital conditions confirmed the superior performance of the TCS. The results exhibited exceptional temperature uniformity, with gradients on the primary and secondary mirrors not exceeding 0.002 °C and 0.017 °C, respectively. The integrated structure–thermal–optical performance analysis quantitatively validated that the achieved thermal stability directly translates to preserved imaging quality. The induced optical aberrations, including misalignments and surface deformations, were minimal, leading to a degradation of the modulation transfer function of less than 2%. This verifies that the thermal design successfully meets the precise thermo-optical requirements of high-resolution hyperspectral imaging.

In conclusion, this research not only delivers a viable thermal solution for a specific advanced payload but also provides a generalized and validated design methodology. The proposed thermal analysis and control strategy offer a foundational blueprint for future micro-satellites and optical instruments, particularly those venturing into non-traditional orbits. Future work will focus on extending this framework to agile satellites with dynamic attitudes and integrating adaptive thermal control technologies for next-generation Earth observation missions. A limitation of this study is that transient thermal analysis was not conducted, and the assessment of thermal robustness and stability is confined to steady-state conditions, without evaluating dynamic temperature responses during component start–stop or orbital transients. Future work will focus on systematic transient thermal simulations and experimental validation to optimize the dynamic temperature control strategy.

Author Contributions: Conceptualization, T.W.; methodology, T.W. and X.Z.; software, Y.X.; validation, X.Z., H.Y. and Y.L.; formal analysis, Y.Z.; investigation, T.W.; resources, T.W.; data curation, Y.X.; writing—original draft preparation, X.Z. and T.W.; writing—review and editing, T.W.; visualization, H.Y.; supervision, T.W.; project administration, T.W.; funding acquisition, T.W. All authors have read and agreed to the published version of the manuscript.

Funding: This research was funded by the National Natural Science Foundation of China, Grant Number: 52505246 and Fundamental Research Funds for the Central Universities, Grant Number: DUT25RC(3)074.

Data Availability Statement: The original contributions presented in this study are included in the article. Further inquiries can be directed to the corresponding author.

Conflicts of Interest: The authors declare no conflicts of interest. The funders had no role in the design of the study; in the collection, analyses, or interpretation of data; in the writing of the manuscript; or in the decision to publish the results.

Abbreviations

The following abbreviations are used in this manuscript:

MHI	Micro-hyperspectral imager
MEOS	Micro Earth observation satellite
TCS	Thermal control system
PM	Primary mirror
SM	Secondary mirror
FPC	Focal plane corrector
STOP	Structure–thermal–optical performance
FEM	Finite element model

FEA	Finite element analysis
ROC	Radius of curvature
MTF	Modulation transfer function
FOV	Field of view

References

1. Rodriguez-Donaire, S.; García-Almiñana, D.; Garcia-Berenguer, M.; Roberts, P.; Crisp, N.; Herdrich, G.; Kataria, D.; Hanessian, V.; Becedas, J.; Seminari, S. Strategic Similarities between Earth Observation Small Satellite Constellations in Very Low Earth Orbit and Low-Cost Carriers by Means of *strategy canvas*. *CEAS Space J.* **2022**, *14*, 767–784. [CrossRef]
2. Zhao, Q.; Yu, L.; Du, Z.; Peng, D.; Hao, P.; Zhang, Y.; Gong, P. An Overview of the Applications of Earth Observation Satellite Data: Impacts and Future Trends. *Remote Sens.* **2022**, *14*, 1863. [CrossRef]
3. Selvadurai, S.; Chandran, A.; Valentini, D.; Lamprecht, B. Passive Thermal Control Design Methods, Analysis, Comparison, and Evaluation for Micro and Nanosatellites Carrying Infrared Imager. *Appl. Sci.* **2022**, *12*, 2858. [CrossRef]
4. Malone, K.J.; Schrein, R.J.; Bradley, M.S.; Irwin, R.; Berdanier, B.N.; Donley, E. Landsat 9 OLI 2 Focal Plane Subsystem: Design, Performance, and Status. In Proceedings of the Earth Observing Systems XXII, San Diego, CA, USA, 6–10 August 2017; p. 5. [CrossRef]
5. Zheng, Y.; Zhang, L.; Song, Y.; Zhang, J.; Lv, X. Low-Rank Reconstruction for Mid-Infrared Spectroscopy Using Broadband Ultra-Wide-Angle Photonic Filters and IReg Algorithm. *Results Phys.* **2024**, *60*, 107622. [CrossRef]
6. Zhang, J.; Zhang, L.; Song, Y.; Zheng, Y. Research on the Spectral Reconstruction of a Low-Dimensional Filter Array Micro-Spectrometer Based on a Truncated Singular Value Decomposition-Convex Optimization Algorithm. *IEEE Photonics J.* **2023**, *15*, 1–10. [CrossRef]
7. Pirondini, F.; López, J.; González, E.; González, J.A. DEIMOS-2: Cost-Effective, Very-High Resolution Multispectral Imagery. In Proceedings of the SPIE Remote Sensing, Amsterdam, The Netherlands, 22–25 September 2014; Volume 9241, p. 92411C. [CrossRef]
8. Zhang, L.; Song, H.; Zan, S.; Liu, H.; Song, Y.; Zhang, F.; Zhu, Y.; Wang, W.; Wang, J.; Sun, K.; et al. Research on System Spectral Response Functions' Calibration and Data Processing Methods for Computational Imaging Spectrometers Based on Filter Modulation. *Measurement* **2024**, *236*, 115120. [CrossRef]
9. Song, H.; Hou, Q.; Sun, K.; Zhang, G.; Xu, T.; Sun, B.; Zhang, L. Parallel Dictionary Reconstruction and Fusion for Spectral Recovery in Computational Imaging Spectrometers. *Sensors* **2025**, *25*, 4556. [CrossRef]
10. Toth, C.; Jóźków, G. Remote Sensing Platforms and Sensors: A Survey. *ISPRS J. Photogramm. Remote Sens.* **2016**, *115*, 22–36. [CrossRef]
11. Wang, T.; Zhang, L.; Zhang, F.; Lu, Y. Reduction and Reconstruction Strategy of Active Thermal Control System Based on Unsupervised Learning and Thermo-Optics for Spaceborne High-Resolution Remote Sensor. *Appl. Therm. Eng.* **2023**, *230*, 120676. [CrossRef]
12. Wang, T.; Zhang, L.; Zhang, F.; Lu, Y. Optimization Strategy of Active Thermal Control Based on Kriging Metamodel and Many-Objective Evolutionary Algorithm for Spaceborne Optical Remote Sensors. *Appl. Therm. Eng.* **2024**, *242*, 122494. [CrossRef]
13. Meng, Q.; Wang, D.; Wang, X.; Li, W.; Yang, X.; Yan, D.; Li, Y.; Cao, Z.; Ji, Q.; Sun, T.; et al. High Resolution Imaging Camera (HiRIC) on China's First Mars Exploration Tianwen-1 Mission. *Space Sci. Rev.* **2021**, *217*, 42. [CrossRef]
14. Guan, F.; Zhang, F.; Cao, N.; Liu, Q.; Liu, J.; Yu, S.; Guan, H. Thermal Control Design and Experimental Verification of Light Off-Axis Space Optical Remote Sensor in the Sun-Synchronous Orbit. *Int. J. Heat Technol.* **2018**, *36*, 125–132. [CrossRef]
15. Fürmetz, M.; Eder, J.; Pfeffermann, E.; Predehl, P. The X-Ray Telescope EROSITA: Qualification of the Thermal Control System. In Proceedings of the SPIE Astronomical Telescopes + Instrumentation, Montréal, QC, Canada, 22–27 June 2014; Volume 9144, p. 91444X. [CrossRef]
16. Huang, W.; Sun, S.; Jiang, H.; Gao, C.; Zong, X. GF-2 Satellite 1m/4m Camera Design and In-Orbit Commissioning. *Chin. J. Electron.* **2018**, *27*, 1316–1321. [CrossRef]
17. Li, S.; Wang, Y.; Zhang, H.; Yu, F. Thermal Analysis and Validation of GF-4 Remote Sensing Camera. *J. Therm. Sci.* **2020**, *29*, 992–1000. [CrossRef]
18. Yang, L.; Li, Q.; Kong, L.; Gu, S.; Zhang, L. Quasi-All-Passive Thermal Control System Design and On-Orbit Validation of Luojia 1-01 Satellite. *Sensors* **2019**, *19*, 827. [CrossRef]
19. Jiang, F.; Wu, Q.; Wang, Z.; Liu, J.; Deng, H. Thermal Design and Analysis of High Power Star Sensors. *Case Stud. Therm. Eng.* **2015**, *6*, 52–60. [CrossRef]
20. Liu, J.; Wang, C.L.; Li, Y.Z. Analysis of Orbital Thermal Environment for Inclined-LEO Small Satellite. *Adv. Mater. Res.* **2014**, *1016*, 446–450. [CrossRef]
21. Wang, T.; Xu, Y.; Ye, H.; Zou, Y.; Lu, Y. Numerical Analysis Method of On-Orbit Dynamic Infrared Radiation Characteristics for Agile Earth Observation Satellites in Non-Track Active Imaging. *Phys. Scr.* **2025**, *100*, 055018. [CrossRef]

22. Bai, T.; Kong, L.; Huang, J.; Jiang, F.; Zhang, L. Thermal Design and Verification of Micro Remote-Sensing Satellite in Low Inclination Orbit. *Opt. Precis. Eng.* **2020**, *28*, 2497–2506. [CrossRef]
23. Wang, T.; Zhang, F.; Xu, Y.; Lu, Y.; Zhang, L. Stability Metering Method for High-Resolution Space Telescope with Large F-Number Based on Combination Optimization. *Optik* **2023**, *277*, 170693. [CrossRef]
24. Wang, T.; Zhang, L.; Jia, X.; Gao, G. Optimized Design of Integrated Ultra-Light Main Supporting Structure for Micro-Nano Remote-Sensing Camera. *Acta Opt. Sin.* **2019**, *39*, 0728009. [CrossRef]

Disclaimer/Publisher's Note: The statements, opinions and data contained in all publications are solely those of the individual author(s) and contributor(s) and not of MDPI and/or the editor(s). MDPI and/or the editor(s) disclaim responsibility for any injury to people or property resulting from any ideas, methods, instructions or products referred to in the content.